

Shadows Wreak Havocs in Transition Disks

YANSONG QIAN¹ AND YANQIN WU¹

¹*Department of Astronomy & Astrophysics, University of Toronto*

ABSTRACT

We demonstrate that shadows cast on a proto-planetary disk can drive it eccentric. Stellar irradiation dominates heating across much of these disks, so an uneven illumination can have interesting dynamical effects. Here, we focus on transition disks. We carry out 3D Athena++ simulations, using a constant thermal relaxation time to describe the disk's response to changing stellar illumination. We find that an asymmetric shadow, a feature commonly observed in real disks, perturbs the radial pressure gradient and distorts the fluid streamlines into a set of twisted ellipses. Interactions between these streamlines have a range of consequences. For a narrow ring, an asymmetric shadow can sharply truncate its inner edge, possibly explaining the steep density drop-offs observed in some disks and obviating the need for massive perturbers. For a wide ring, such a shadow can dismantle it into two (or possibly more) eccentric rings. These rings continuously exert torque on each other and drive gas accretion at a healthy rate, even in the absence of disk viscosity. Signatures of such twisted eccentric rings may have already been observed as, e.g., twisted velocity maps inside gas cavities. We advocate for more targeted observations, and for a better understanding on the origin of such shadows.

1. INTRODUCTION

Over the past decade, high resolution observations have revealed a wide variety of sub-structures in proto-planetary disks, including cavities (Long et al. 2018), rings (ALMA Partnership et al. 2015), arcs (van der Marel et al. 2013) and spirals (Kurtovic et al. 2018). Such features are likely closely related to planet formation, but it remains unclear if planets are the cause or the effect.

A prominent type of sub-structures is an inner cavity. Disks with this morphology, known as transition disks, can often be recognized from their spectral energy distribution (Strom et al. 1989; Calvet et al. 2002), as the inner clearing leads to a deficit in infrared radiation (for reviews of transition disks, see Espaillat et al. 2014; Owen 2016; van der Marel 2023a). The origin of these cavities is currently unclear. While planetary perturbers are often invoked, simulations have found that even multiple planets have difficulties in opening wide and deep gaps (Zhu et al. 2011). The discovery of transition disks in very young sources (Sheehan & Eisner 2017) also places more strain on the planet hypothesis.

In addition to an unclear origin, transition disks also present other puzzles. For instance, they commonly exhibit sharp inner edges (e.g., van der Marel

et al. 2015a; Dong et al. 2017). In the ring of MASS J16042165–2130284 (shortened as J1604 in this work), densities of big dust, small dust and possibly gas drop by a few orders of magnitudes over a distance less than 10au, or a couple local scale heights (Dong et al. 2017). Other transition disks also show similarly sharp density cutoffs (see, e.g. Brown et al. 2009; van der Marel et al. 2015b). Planets, especially multiple planets, tend to carve only shallow cavities (Duffell 2015).

Similarly surprising is the on-going gas accretion. Despite inner cavities that sometimes extend to tens of AUs, the accretion rates reported for these systems are comparable to those of full disks (Manara et al. 2014; van der Marel 2023a). To maintain such accretion rates, gas in the evacuated regions has to lose angular momentum rapidly and falls inward with transonic or free-fall velocities (Rosenfeld et al. 2014; Wang & Goodman 2017). This requires efficient loss of angular momentum, and theories involving magnetized winds (Wang & Goodman 2017) or planetary perturbations (Goodman & Rafikov 2001) have been proposed.

Motivated by these observations, we explore one physical ingredient that has so far been largely overlooked: disk shadows.

Temperature and pressure in much of a proto-planetary disk are supplied by stellar irradiation (Kenyon & Hartmann 1987; Chiang & Goldreich 1997). As such, any perturbations in stellar illumination can

have dynamical consequences (see, e.g. Watanabe & Lin 2008; Wu & Lithwick 2021).

At the same time, azimuthal shadows are commonly detected in scattered light of transition disks. For example, the outer ring of J1604 shows two roughly opposed shadows (Pinilla et al. 2015; Mayama et al. 2018). These shadows are highly variable, even down to day timescales (Pinilla et al. 2018a). Moreover, the pair of shadow is asymmetric in their depths. Similarly, shadow asymmetry is also reported for the TW Hya disk, one of the best monitored disks, where the two occulting shadows are located on the same half of the circle (Debes et al. 2023).

Shadows are also reported in thermal radiation of transition disks (e.g., van der Marel 2023b; Arce-Tord et al. 2023) and in chemical (C/O ratio) pattern (Keyte et al. 2023; Temmink et al. 2023). So observational evidences are mounting that shadows, and in particular asymmetric shadows, are an integral part of a disk’s environment.

These shadows are commonly attributed to misaligned inner disks (e.g., Marino et al. 2015; Benisty et al. 2017), though such a scenario may not explain the rapid variabilities that are observed (in both magnitudes and locations). Variable accretion stream in the stellar magnetosphere is another possibility (Romanova et al. 2013).

Regardless of the origin of shadows, they will affect the thermodynamics and therefore the dynamics of transition disks. Previously, the role of symmetric shadows has been investigated by the group of Montesinos et al. (2016); Montesinos & Cuello (2018); Cuello et al. (2019) using 2D simulations. In this work, we study the response of a gas ring under a time-independent, asymmetric shadow, using 3D Athena++ simulations (Stone et al. 2020). In §2, we describe our physical model and numerical setup. We present our results in §3, interspersed with physical explanations and comparison against other works. We discuss in §4 the observational consequences.

2. METHODS

We perform 3D hydrodynamics simulations using Athena++ (Stone et al. 2020).

Many of our parameter choices are motivated by the J1604 disks, which shows a sub-mm ring at ~ 70 au, but shines the brightest in scattered light at ~ 60 au. The half width of the ring is ~ 10 AU (Dong et al. 2017). Pinilla et al. (2018a) found that the two shadows, when viewed in reflected light, are roughly opposed, though their separation can vary from 150° to 190° . The shadows also show time-varying and asymmetric depths: the eastern shadow has an amplitude that varies from 40%

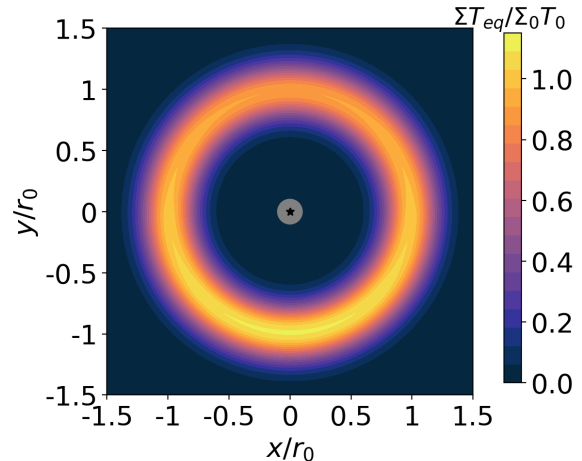


Figure 1. figure illustrating the ring and its $m = 1$ shadow. The color indicates the product of the surface density (eq. 1) and the imposed temperature (T_{eq} , eq. 6). The latter has a 10% $m = 1$ perturbation on top of the axisymmetric form. The central grey circle represents the inner boundary.

to 90%, while its counterpart varies from 30% to 95%. The difference between these amplitudes can be as large as 30%.

2.1. The Disk and Its Shadow

We start with an axisymmetric disk. The gas surface-density is assumed to be ring-like,

$$\Sigma(r) = \Sigma_0 \exp \left[-\frac{(r - r_0)^2}{2\sigma_r^2} \right], \quad (1)$$

where $\Sigma_0 = \Sigma(r = r_0)$ and σ_r is the ring width. We choose it to be $0.16 r_0$ in the fiducial model.¹ The total disk mass is $(2\pi)^{3/2}\sigma_r\Sigma_0$. Computationally, simulating such a ring profile (as opposed to a full disk) has the advantage that any boundary effects from the inner and outer boundaries are minimized.

The initial vertical density distribution follows that of a vertically isothermal disk in hydrostatic equilibrium,

$$\rho(r, z) = \frac{\Sigma(r)}{\sqrt{2\pi} h(r)} \exp \left[-\frac{z^2}{2h(r)^2} \right], \quad (2)$$

where the gas scale height $h(r) = c_s/\Omega$, with $\Omega = \sqrt{GM_*/r^3}$ being the Keplerian frequency and $c_s = \sqrt{k_B T/\mu m_H}$ the isothermal sound speed. The local temperature initially scales with radius as

$$T = T_{bg}(r) = T_0 \left(\frac{r}{r_0} \right)^{-1/2}. \quad (3)$$

¹ This corresponds to ~ 10 AU if $r_0 = 60$ AU. Moreover, for our chosen parameters, this corresponds to ~ 2 vertical scale heights at $r = r_0$.

We choose a value for T_0 such that $(h/r)_{r_0} = 0.084$.

The initial velocity profile follows that of pure rotation, with the azimuthal velocity satisfying the radial force balance at all heights:

$$\frac{v_\phi^2}{r} = \frac{GM_*}{r^2} + \frac{1}{\rho} \frac{dP}{dr}, \quad (4)$$

where P is the ideal gas pressure, $P = k_B \rho T / \mu m_H$.

Stellar irradiation is treated in a simple fashion in this initial exploration. The amount of illumination is quantified by the so-called equilibrium temperature, $T_{\text{eq}}(r, \phi)$. This is inserted into the energy equation of **Athena++** as an extra heating source:

$$\left(\frac{dE}{dt} \right)_{\text{irradiation}} = -\frac{1}{\tau_c} \frac{\rho k_B (T - T_{\text{eq}})}{(\gamma - 1) \mu m_H}, \quad (5)$$

where $\gamma = 5/3$ is the adiabatic index² and we introduce the lag time, τ_c , to describe the response of the disk to a time-varying illumination. We adopt a constant relaxation time of $\tau_c = 0.1 P_0$, where P_0 is the Keplerian orbital time at r_0 . The disk is also assumed to remain vertically isothermal at all times.

Our two assumptions, a short thermal relaxation time, and a vertical isothermal condition, are not appropriate for the main ring of J1604. The disk's thermal inertia is high there due to the high dust density. These assumptions are more realistic inward of the main ring where the density is lower and where the scattered light is at the brightest. Here, the disk is vertically optically thin to its own thermal radiation, and radially optically thick to star light (see, e.g. [Wu & Lithwick 2021](#)). This region, by definition, is also where most of the stellar heating is absorbed and so is the most dynamically relevant region.

The azimuthal shadow can now be easily accommodated by a ϕ -dependent T_{eq} . We assume the shadows are fixed in inertial space. We also simplify the matter by studying only one particular form of shadow. Any complicated shadows (e.g., one shadow, two symmetric ones, two asymmetric ones, broad, narrow) can be decomposed into individual Fourier components ($e^{im\phi}$ with $m = 1, 2, \dots$). We find that the only Fourier component of interest is the $m = 1$ term (see §3.6 for a study of the symmetric $m = 2$ term). So we write

$$T_{\text{eq}}(r, \phi) = T_{\text{bg}}(r) (1 - \epsilon \sin \phi). \quad (6)$$

The temperature minimum and maximum lie at $\phi = \pi/2$ and $3\pi/2$, respectively. We set $\epsilon = 0.1$. This is compatible with the shadow asymmetry observed in J1604

([Pinilla et al. 2018a](#)), as well as that in TW Hya ([Debes et al. 2023](#)).

2.2. Numerics

The simulation is performed in spherical coordinates, $\{r, \theta, \phi\}$, with $60 \times 42 \times 180$ grids respectively. In the radial direction, the domain is $r \in [0.1 r_0, 2.5 r_0]$, and the size of each cell increases by a factor of 1.04 in ascending order. The polar grid is evenly spaced in $\theta \in [\frac{1}{2}\pi - 0.5, \frac{1}{2}\pi + 0.5]$. This ensures that we cover at least 3 scale heights from the midplane for the entire disk. The azimuthal grid is evenly spaced in $\phi \in [0, 2\pi]$.

As we follow the gas up to multiple scale heights above the mid-plane, gas density in our 3D simulations has a very large dynamic range. It is common and necessary to assert floor values for density and pressure. We set them to be 10^{-9} and 10^{-12} of the mid-plane values at r_0 .

For the radial and polar coordinates, boundary conditions are specified in **Athena++** by the ghost cells at the boundaries. We set $v_r = v_z = 0$ at all ghost cells, to prevent gas inflow and outflow. Some attention is required at the top and bottom polar boundaries where densities are exceedingly low. Due to our adoption of a density floor, which violates the condition for hydrostatic equilibrium, waves are continuously excited in these regions. We follow [Kutra et al. \(2023\)](#) to mitigate this partially. We assign densities to the ghost cells as logarithmic extrapolation of the two adjacent cells. Moreover, the azimuthal velocities and temperatures are fixed to the initial values for these top/bottom ghost cells. For the ϕ direction, we adopt periodic boundary conditions.

We set a minimum CFL number of 0.3 and integrate the model for 250 orbital time at r_0 (P_0). This is equivalent to ~ 0.1 Myr if the ring is located at 60 AU around a solar mass star.

3. RESULTS

Here, we will describe the results of our simulations, interspersing it with discussions of the underlying physics. We find that asymmetric shadows drive the ring to become eccentric, which then leads to disk truncation and accretion. In contrast, symmetric shadows have no dynamical impacts.

3.1. Becoming Eccentric

[Fig. 2](#) depicts how the gas streamlines evolve with time, after the asymmetric shadow is turned on. The most striking feature is that the streamlines become eccentric.

To understand this reaction, we consider one fluid element moving in orbit. As it enters and exits the

² A more appropriate value for molecular gas is $\gamma = 7/5$. But this is of no consequence here.

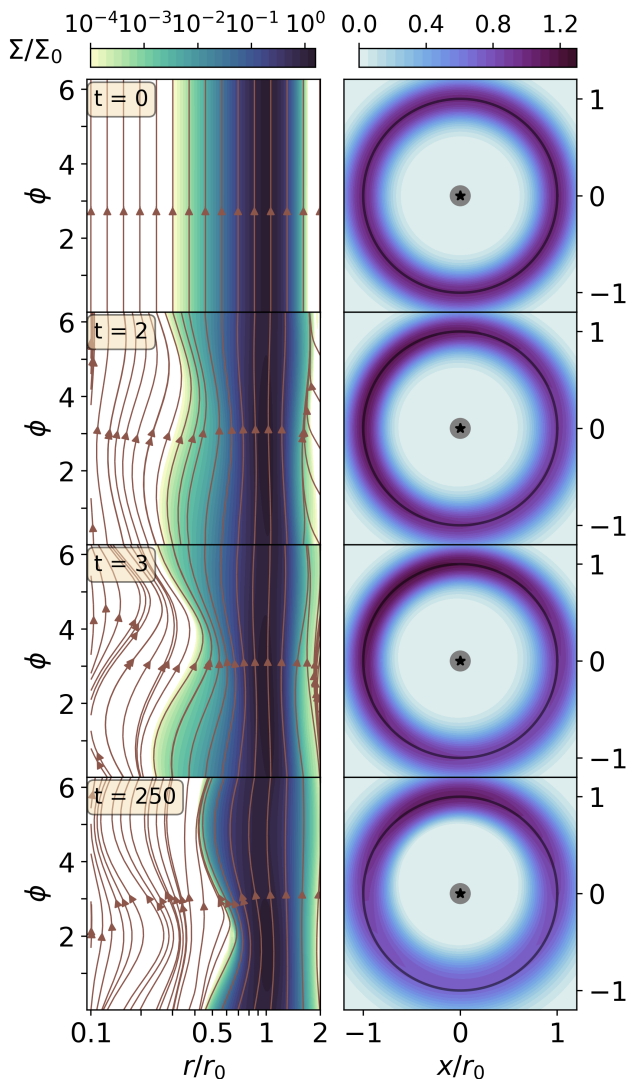


Figure 2. Four snapshots of the evolution for our fiducial ring, with time measured in unit of P_0 . On the left, the colored contours illustrate logarithmic surface densities (scaled by Σ_0) in cylindrical coordinates, while the brown curves are the fluid streamlines. On the right, the colored contours illustrate the linear surface densities (again normalized by Σ_0) in Cartesian coordinates. An initially circular and narrow ring reacts to the $m = 1$ shadow by becoming eccentric. The eccentricity growth is complete after about a dozen P_0 , with the final streamlines being a set of twisted eccentric ellipses. Some streamlines cross each other and truncate the disk sharply in the inner edge.

shadow, its temperature is modified, by an amount that depends on how fast it is moving and how quickly it reacts to the local forcing temperature (T_{eq}). Ignoring changes in density and velocity, eq. 5 can be recast as one for the fractional temperature perturbation,

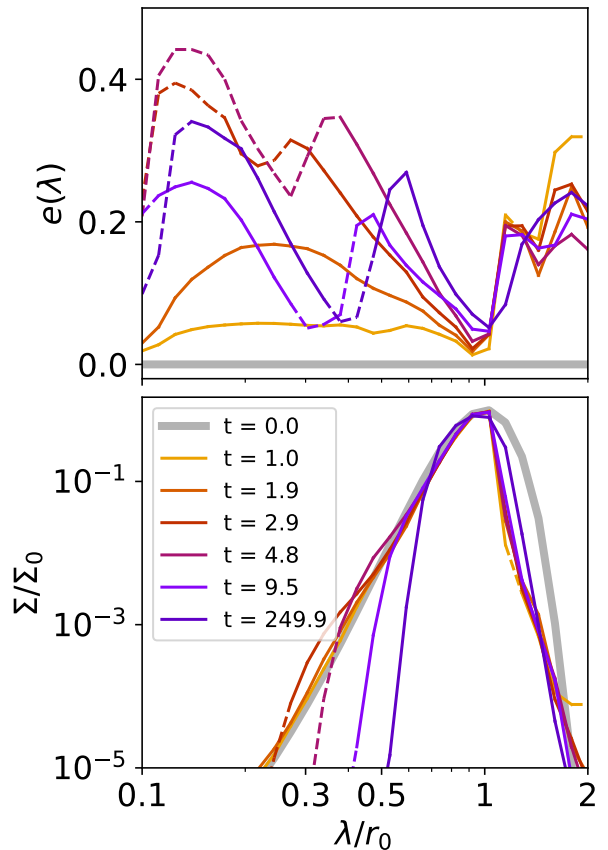


Figure 3. Evolution in eccentricity (upper panel) and surface density (lower) for the narrow, circular ring in Fig. 2. The horizontal axis is now replaced with the semi-latus rectum λ (eq. 12), a more appropriate coordinate for an eccentric disk. All results are averaged over the azimuth angle. The initial profiles are plotted as thick grey curves, while the colored curves are later snapshots. Dashed parts indicate regions where the streamlines cross ($\partial r/\partial \lambda \leq 0$). The disk quickly becomes eccentric, and within a dozen orbits, streamlines crossing has evacuated the inner region and truncated the disk sharply at $\sim 0.6r_0$.

$$\delta T/T = (T - T_{\text{bg}})/T_{\text{bg}},$$

$$\frac{d}{dt} \left(\frac{\delta T}{T} \right) = -\frac{1}{\tau_c} \left(\frac{\delta T}{T} \right) - \frac{1}{\tau_c} \epsilon \sin \phi. \quad (7)$$

We write $\phi = \Omega t$, so the forcing term (second term on the right hand side) scales as $\mathcal{R}(e^{i\Omega t - i\pi/2})$, where \mathcal{R} indicates taking the real part. We look for a periodic solution of the form $(\delta T/T) \propto e^{i\Omega t}$. Simple manipulation yields

$$\frac{\delta T}{T} = \left[\frac{\epsilon}{\sqrt{1 + (\Omega\tau_c)^2}} \right] \mathcal{R} \{ e^{i\Omega t + i\phi_0} \}, \quad (8)$$

where ϕ_0 is the phase delay, $\phi_0 = \arccos[\frac{\Omega\tau_c}{(1+(\Omega\tau_c)^2)^{1/2}}]$. So the response magnitude is the largest when $\Omega\tau_c \ll 1$,

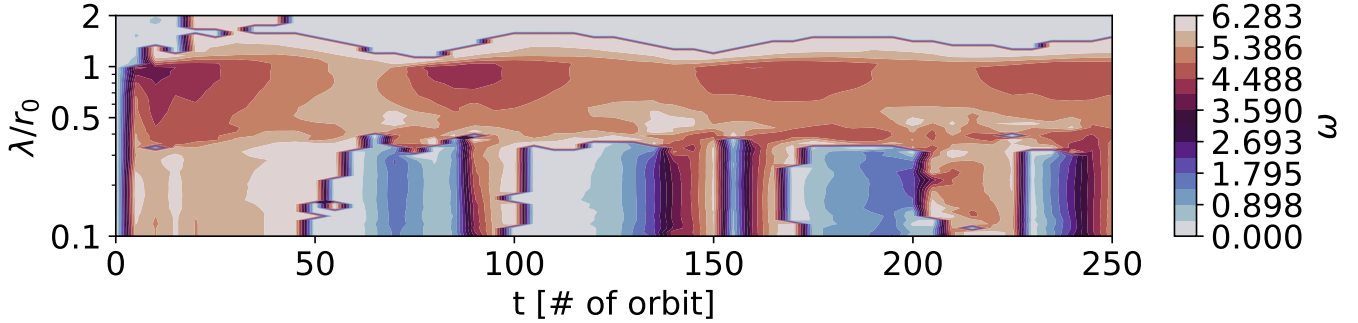


Figure 4. Evolution in the argument of periapsis (colors indicate ω) throughout the disk. The asymmetric shadow forces different streamlines to orient differently. Regions of the disk that develop sharp gradients in eccentricity and argument of periapsis are most susceptible for streamline crossing. The ring is quickly truncated there. During the quasi-steady state (after a dozen P_0), the ring continues making periodic adjustments. See text.

or when the disk has a low density. Moreover, with our choice of $\tau_c = 0.1P_0$, the temperature response is nearly instantaneous at $r \geq r_0$ ($\Omega\tau_c \ll 1$), but is significantly delayed at $r \ll r_0$. This leads to elliptical streamlines that differ in their orientations (twisted).

The above temperature response modifies the radial pressure gradient, and causes the fluid elements to converge toward or to expand away from the ring centre, where gas pressure is at a maximum. In this way the $m = 1$ illumination pattern excites radial epicyclic motion resonantly, driving the disk to become eccentric. In contrast, an $m = 2$ pattern is not effective (see Appendix).

The magnitude of the response also depends on the background density gradient. Ignoring density changes and terms that vary slowly on scale of radius, we can simplify the radial momentum equation as

$$\frac{\partial v_r}{\partial t} \approx -\frac{1}{\rho} \frac{\partial(\rho\delta T)}{\partial r} = -\delta T \frac{d \ln \rho}{dr}. \quad (9)$$

So the eccentricity ($e \sim v_r/v_{\text{kep}}$) is driven the fastest where $\delta T/T$ is the highest (eq. 8), and where the background density gradient is the sharpest. Our narrow ring with $\sigma_r \ll r$ provides the latter condition.

3.2. Nonlinear Development of the Eccentric Ring

While the above hand-waving arguments explain why and how the disk becomes eccentric, the global and nonlinear behaviour of the disk is much less straightforward to understand. Our numerical simulations provide guidance. To analyze eccentric disks, we measure the eccentricity vector at every point by

$$\mathbf{e}(r, \phi) = \left(\frac{|\mathbf{v}|^2}{\mu} - \frac{1}{|\mathbf{r}|} \right) \mathbf{r} - \frac{\mathbf{r} \cdot \mathbf{v}}{\mu} \mathbf{v}, \quad (10)$$

where $\mu = GM_*$. The direction of this vector points towards the periapsis, the argument of which can be

measured as

$$\omega(r, \phi) = \phi - \arccos \frac{\mathbf{e} \cdot \mathbf{r}}{|\mathbf{e}||\mathbf{r}|}. \quad (11)$$

The (r, ϕ) coordinates are not convenient for eccentric orbits. We follow Ogilvie (2001) to introduce a new set of coordinates, (λ, ν) , where λ is the semi-latus rectum $\lambda = a(1 - e^2)$, and ν is the true anomaly $\nu = \phi - \omega$. The coordinate transformation follows the polar equation of ellipse:

$$r(\lambda, \phi) = \frac{\lambda}{1 + e(\lambda) \cos \nu(\lambda, \phi)}. \quad (12)$$

The new set (λ, ν) are better labels for eccentric orbits, as λ is exactly conserved along a Keplerian orbit and approximately so for continuum fluid. We can now proceed to plot results as functions of λ only.

Figs. 2-3 show how the eccentricity and surface density evolve in our narrow ring case. The disk reaches maximum eccentricities within a few orbits. The centre of the ring remains circular, as expected (eq. 9), while the two flanks become eccentric. The disk now appears as a nested set of twisted ellipses (eq. 8).

Such streamlines interact. One extreme form of interaction is streamline crossing. This occurs when the derivative, $\partial r / \partial \lambda$ falls below zero, where

$$\frac{\partial r}{\partial \lambda} = \frac{1}{(1 + \cos \nu)^2} \left[1 + \left(e - \frac{\partial e}{\partial \ln \lambda} \right) \cos \nu - e \frac{\partial w}{\partial \ln \lambda} \sin \nu \right] \quad (13)$$

measures the compactness of streamlines, with $\partial r / \partial \lambda = 1$ for circular Keplerian orbits. This expression suggests that both the eccentricity gradient and the twist bring about streamline crossing.

As one observes in Fig. 3, the low density region of the ring suffers the most from streamline crossing (marked by dashed curves). Within a dozen periods, this region

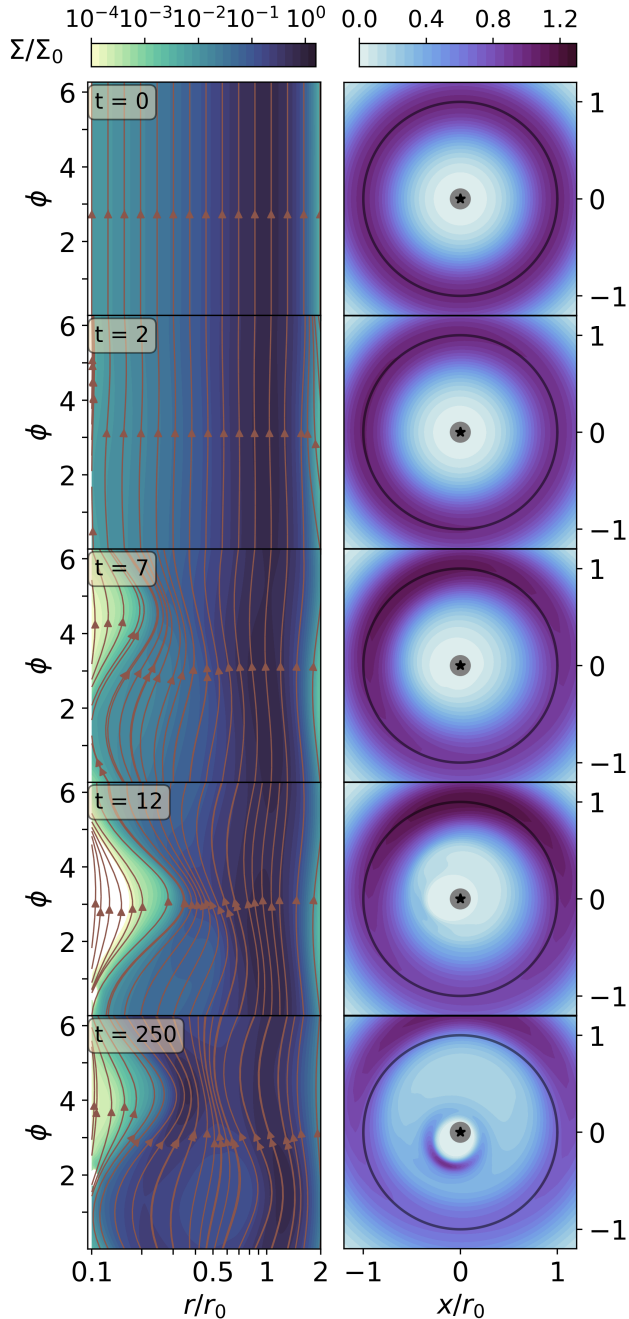


Figure 5. Similar to Fig. 2 but for a wider ring ($\sigma_r = 0.3r_0$). The growth of eccentricity takes longer, and a steady state is reached after about $100P_0$. The ring is now split into two separate eccentric rings that have nearly opposite arguments of periapsis. The intermediate region is evacuated and has a density that is lower by order unity. Interactions between the two eccentric rings drive continuous mass accretion.

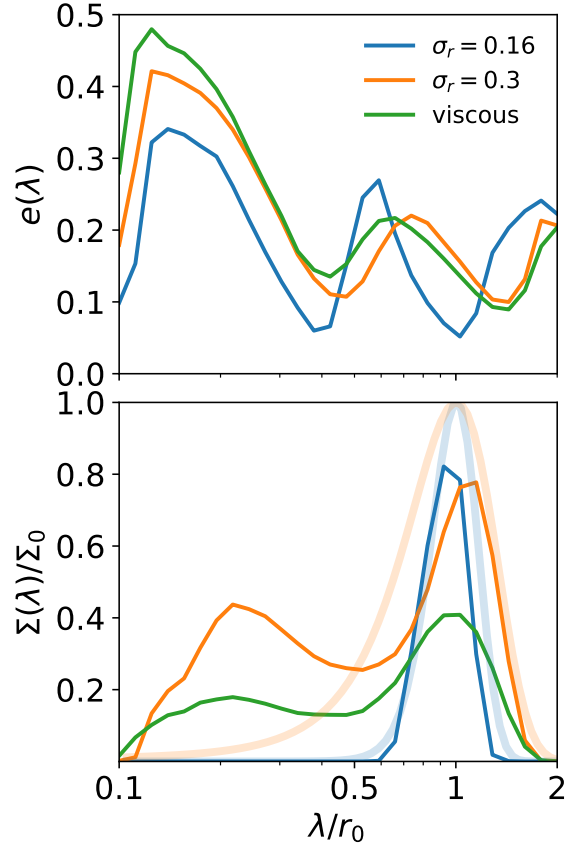


Figure 6. Final eccentricity (upper panel) and surface density (lower panel) profiles for three simulations: inviscid narrow ring ($\sigma_r = 0.16r_0$), inviscid broad ring ($\sigma_r = 0.3r_0$), and viscous narrow ring ($\sigma_r = 0.16r_0$). Initial configurations are shown as thick light curves. All rings reach similar eccentricity profiles. Their surface densities are more different. Unlike the narrow inviscid case which shows a sharp truncation, the wide inviscid ring is broken apart into two separate rings. At the addition of viscosity, the narrow ring spreads and reaches the same state as that of the broad inviscid ring.

is evacuated, and we are left with a ring that is sharply truncated (more below).³

Afterwards, the disk settles into a quasi-steady state. The eccentricity pattern holds steady, with a minimum at r_0 ; the inner and outer halves of the ring have opposite arguments of periapsis (Fig. 4). This is likely the long-lived state of the ring when under both internal stress and external forcing (Ogilvie 2001; Statler 2001). However, we observe that the disk is not perfectly steady. Instead, the eccentricity vectors fluctuate with a period of $\sim 75P_0$. This is because the eccentric

³ The same dynamics may also be at play for the outer part. But our results there may be polluted by the proximity of the outer boundary.

disk naturally precesses, but the forcing by the shadow does not allow it. So the disk behaves like a harmonic oscillator that is being forced away from resonance.

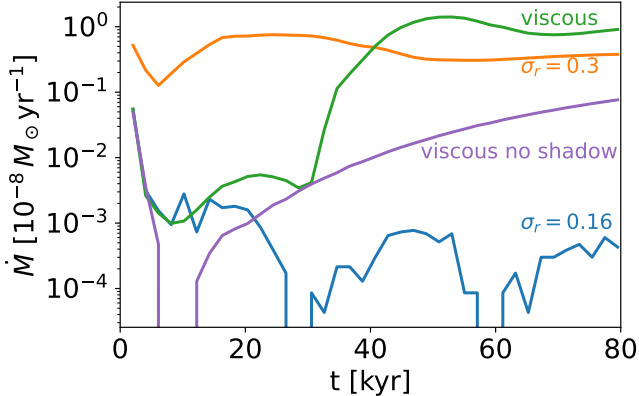


Figure 7. Mass accretion rates as functions of time in various models. Here, \dot{M} is measured by the change in total mass that remains outside $0.4r_0$. Three of the cases are those in Fig. 6, and we add a fourth case of viscous narrow ring without shadow forcing. We assume a total disk mass of $10^{-2} M_\odot$, $r_0 = 60$ AU, $\alpha = 10^{-3}$ at r_0 , and simulate for $250P_0$. We find that asymmetric shadows alone can cause accretion (see the wide invisid case), and that in the presence of viscosity, it can significantly boost accretion (compare ‘viscous’ vs ‘viscous no shadow’).

3.3. Disk Sculpting

Here, we focus on the effects of disk sculpting. Fig. 3 makes clear that the $m = 1$ shadow truncates the narrow ring into one that has sharp edges. We find that the surface density drops off by more than 4 orders of magnitude just inward of $0.6r_0$, with a decaying length of order (and slightly smaller than) the local scale height. Such disks are on the verge of Rayleigh instability (Papaloizou & Lin 1984; Yang & Menou 2010). So even a weak shadow is able to carve out a very sharp edge.

In this case, since our ring starts narrow, the amount of mass that is carved away (and accreted) is only a tiny fraction of the disk mass. In the following, we provide an even more dramatic demonstration of the shadow carving by simulating an initially wider ring, $\sigma_r = 0.3r_0$.

The results for such a ring are shown in Fig. 5 and Fig. 6. Eccentricity growth in a wider ring proceeds more slowly, due to the more gentle density gradient (eq. 9). We find that a quasi-steady state is reached after $\sim 100P_0$, with an eccentricity profile that is similar to that of the narrow ring (Fig. 6). The surface density profile, on the other hand, looks different. We observe that the broad ring is now broken up into two separate rings with comparable surface densities.

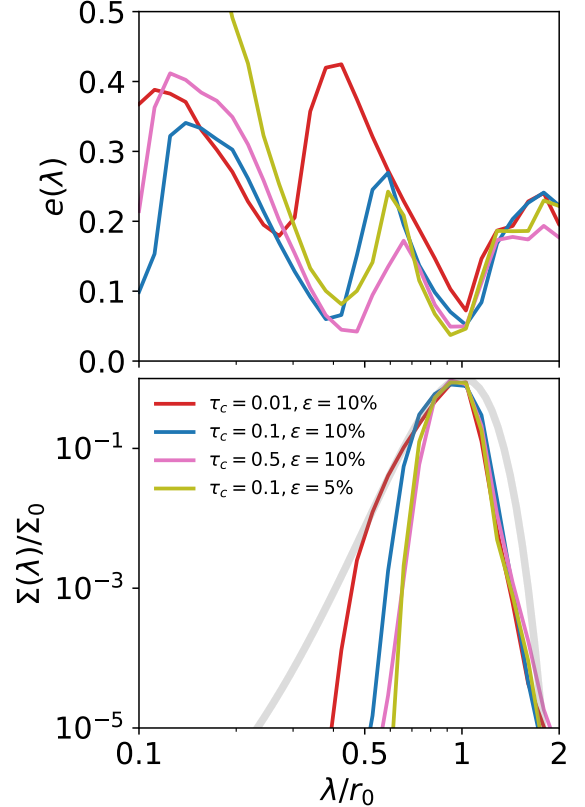


Figure 8. Final eccentricity and surface density for the narrow ring case, now with different thermal relaxation times and driving amplitudes. The light grey curve indicates the initial state. All rings reach similar quasi-steady states as that of our fiducial case ($\tau_c = 0.1P_0$, $\epsilon = 10\%$), namely, similar eccentricity values in the bulk of the ring, and similarly sharp truncation.

This occurs because the inner and the outer rings are twisted relative to each other (eq. 8). Any gas in the intermediate region suffers severe streamline crossing. It is then whisked away and piled up instead in the inner ring. Fig. 5 shows that, even at steady state, the two rings continue to interact: the apoapsis of the inner ring rubs against the periapsis of the outer ring and sound waves are excited. This continuous friction leads to an interesting consequence: accretion. We discuss this below.

In summary, an $m = 1$ shadow can truncate a narrow ring sharply, and can break a wider disk into discrete rings that are eccentric and interacting.

3.4. Disk Accretion

Fig. 7 presents the gas accretion rate for a few different simulations. To minimize effects of the inner boundary, we measure the mass accretion rate at $r = 0.4r_0$.

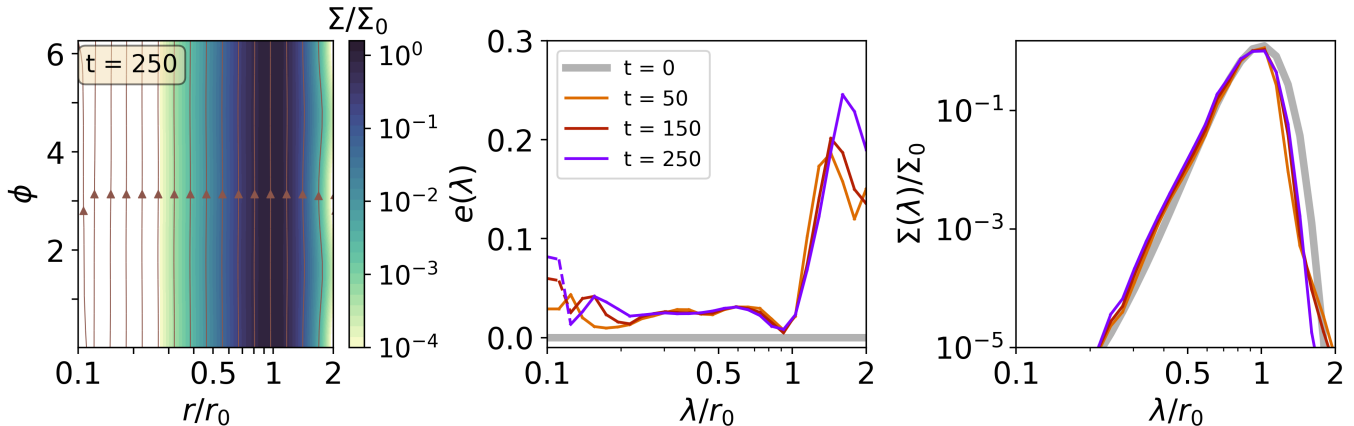


Figure 9. Evolution of the narrow ring under a symmetric shadow (eq. 14). The left panel shows the final streamlines. The ring remains largely circular. The middle and right panels show a few snapshots of the eccentricity and surface density profiles. Unlike for the case of an asymmetric shadow, eccentricity remains negligible and the surface density remains unchanged.

For our narrow inviscid case, accretion is minimized (but non-zero) after the ring has reached the quasi-steady state. However, a healthy rate of accretion is maintained in the wide inviscid case, despite the absence of viscosity. The continuous ‘rubbing’ between the twisted inner and outer rings causes repetitive compression and decompression of the streamlines, much like Sisyphus and his impossible task of rock lifting. This transports angular momentum and, as we find here, leads to accretion. We find that the accretion rate is comparable to that of a standard α -disk (see below).

Even when the disk is viscous, shadow forcing dramatically enhances the accretion. We demonstrate this by simulating the narrow ring with viscosity, and compare the cases with and without shadow forcing. We adopt a constant kinematic viscosity of $\nu = 10^{-5}$ (in code unit), which corresponds to a conventional α parameter of $\alpha \sim 10^{-3}$ at r_0 and $\sim 10^{-2}$ at $0.1r_0$ (Shakura & Sunyaev 1973). The shadowed ring accretes at a rate that is about five times higher. The accretion is likely enhanced by the sharp density gradient that an asymmetric shadow produces.

3.5. Parameter Dependence

Our results depend on two important parameters: the thermal relaxation time, τ_c , and the amplitude for shadow forcing, ϵ .

In Fig. 8, we present the final eccentricity and surface density profiles when the values of τ_c and ϵ are modified from our fiducial ones. To our surprise, we find that the final states are not sensitive to these parameters.

We have expected these parameters to affect the magnitudes of temperature perturbations (eq. 8), producing weaker responses when τ_c is longer, and when ϵ is smaller. And we do observe that in simulations, rings

take longer to build up their eccentricities if τ_c are larger and if ϵ are smaller. However, when these rings reach their quasi-steady states, their eccentricity profiles for the main ring (near r_0) look largely invariant. All disks are also truncated with a similar sharpness.

We suspect this convergence is the result of nonlinear evolution. The shadow forcing saturates at the same final configuration, regardless of the amplitude of forcing. These results should be followed up with more in-depth investigations. Meanwhile, it gives us some confidence that our results are not sensitive to the choice of the parameters.

3.6. Symmetric Shadows: comparison with other Studies

Here we first show that symmetric shadows do not drive eccentricity. As symmetric shadows are the default set-up in a number of previous studies and a variety of dynamical effects have been reported for them, we discuss the discrepancy.

For the symmetric shadow, we assume it to consist of two Gaussian troughs at 0.5π and 1.5π respectively:

$$T_{eq}(r, \phi) = T_0 \left(\frac{r}{r_0} \right)^{-\frac{1}{2}} \times \left\{ 1 - \epsilon \exp \left[-\frac{(\phi - 0.5\pi)^2}{2\sigma_\phi^2} \right] \right\} \times \left\{ 1 - \epsilon \exp \left[-\frac{(\phi - 1.5\pi)^2}{2\sigma_\phi^2} \right] \right\}. \quad (14)$$

In terms of Fourier components, this shadow can be decomposed into $m = 2, 4, 6, 8, \dots$ components. We choose a shadow-width $\sigma_\phi = 0.3$ and a relatively large shadow-depth of $\epsilon = 0.6$. The ring is radially narrow with $\sigma_r = 0.16$. Fig. 9 shows the evolution (or rather, the lack of) under this shadow. The ring stays largely circular and the surface density profile remains unchanged.

The eccentric mode is suppressed because the forcing imposed by symmetric shadows is not resonant with the orbit.

These results contrast with those reported by previous studies, all of which focus only on symmetric shadows and employs 2D simulations (vertically integrated equations).

Montesinos et al. (2016) simulated the effects of a pair of symmetric shadows on a continuous disk instead of the ring. Their very deep shadows (blocking out 0.999 of the starlight) can excite shallow density spirals, when the disk is gravitationally unstable, or when the stellar luminosity is unphysically high. In contrast, there is little effect when the disk is low in mass or when the stellar luminosity is modest. This is consistent with our results here.

Later studies from the same group invoke additional effects like slowly precessing symmetric shadows (Montesinos & Cuello 2018), or back-reaction from dust particles on the shadowed disk (Cuello et al. 2019). These appear to produce interesting effects but are not in direct contradiction with our results.

Lastly, a preprint appeared at the same time as our work (Su & Bai 2024). These authors simulated disks with a wide range of physical parameters. They found that symmetric shadows on continuous disks (not rings) can trigger structures like spirals, rings and crescents. It is hard to understand the difference between our conclusions and theirs, before one develops a clear physical explanation for the reported effects. In the meantime, we speculate that both nonlinearity (deep as opposed to the shallow shadows studied here) and boundary effects (continuous disks experience the inner boundary) may play some roles.

4. CONNECTIONS TO OBSERVATIONS

Our exploratory study reveals the surprising benefits of an asymmetric shadow. In the following, we speculate on possible connections to the observed systems.

4.1. *Disk Sculpting*

We return to the issue of sharp inner edges. Disk shadows, even with an asymmetry of order a few percent, can sharply truncate a ring within tens of orbits. In our narrow ring case, the density at the edge falls off by many orders of magnitude, with a characteristic scale that is the local scale height. This can be maintained for as long as the shadows are present. This could help explain systems like J1604 and others (see Intro) without the need to invoke massive companions.

In addition to sharp truncation, our simulations also show that a wide ring can be dismantled into two pieces

with comparable surface densities. It is also possible, if we are able to simulate a larger radial domain, that an initially smooth disk can be shattered into multiple rings. Such multiple ring system are commonly observed in high resolution images, with famous examples like HL Tau (ALMA Partnership et al. 2015), AS 209 (Huang et al. 2018) and TW Hya (Andrews et al. 2016). Whether shadow is the main cause of these substructures require more investigations.

4.2. *Eccentric disk*

There are at least two known eccentric disks. Both MWC 758 and AB Aur are confirmed to be eccentric and off-centered in mm wavelengths (Dong et al. 2018; van der Marel et al. 2021). MWC 758, in particular, has a measured eccentricity of 0.1, similar to what we find in simulations (Fig. 6). A few more candidates of eccentric transition disks are recently revealed by Jensen et al. (2023) from spectro-astrometric observations of CO ro-vibrational lines.

If eccentric transition disks are wide-spread, asymmetric shadows provide a universal mechanism that is natural and efficient. In this case, we predict that disk eccentricities tend to be greater further away from the ring centre, and the arguments of periapsis are not aligned. These could be tested by observations of dust and gas. In this regard, the recent report of an asymmetric ring around CIDA 9A (Harsono et al. 2024) gives one the hope that high-resolution, multi-wavelength observations would be soon available to test the shadow hypothesis.

Lastly, the dynamics of grains in such eccentric disks is worth investigating. For grains that are not strongly coupled to the gas, they may not follow the gas streamlines closely. There can be complicated gas-dust interactions (strong wind, fragmentation, drifting) in eccentric disks.

4.3. *Accretion in Transition Disks*

If transition disk objects do accrete at healthy rates, material in the central cavities would have to lose angular momentum rapidly and move inwards at appreciable speeds. Interacting streamlines, forced by asymmetric shadows, can either act as the agent of friction itself (as in our wide ring inviscid case), or as the facilitator for viscosity (as in our narrow viscous case).

Shadow forcing has another advantage over alternative scenario like magnetized wind (Wang & Goodman 2017) or planetary perturbations (Goodman & Rafikov 2001). It can work at all radii where shadows are cast, i.e., over many decades in orbital separations.

Streamline crossing occur likely at supersonic speed. If this is present in disk cavities, one can hope to find signatures in grain sublimation and gas emissions.

4.4. Kinematic Signatures

The eccentric streamlines should also be observable in kinematically resolved line emissions.

In the centre of many transition disks, line emissions are found to be distorted in the so-called intensity-weighted velocity maps (moment-1 maps). These include, e.g. HD 100546 (Walsh et al. 2017), DoAr 44 (Antilen et al. 2023), an SY Cha (Orihara et al. 2023). Fig. 10 presents the case of J1604, where both the CO (3-2) and HCO^+ (4-3) moment-1 maps show a twisted structure inside the cavity (Mayama et al. 2018).

This feature has been interpreted as due to warped inner disks (Loomis et al. 2017; Juhász & Facchini 2017), or due to fast radial inflow (Rosenfeld et al. 2014). We suggest here that it could also result from eccentric streamlines in an inclined disk.

We produce a theoretical image for visual comparison. We adopt the final snapshot of the wide ring case ($\sigma_r = 0.3$). We then calculate the projected line-of-sight velocity:

$$v(x', y') = v_\phi \sin i \sin \phi - v_r \sin i \cos \phi, \quad (15)$$

in the frame $(x', y') = (x \cos i, y)$ where i is the disk inclination and ϕ the azimuth angle. The left panel of Fig. 10 shows the projected midplane velocity when $i = 6^\circ$, the estimated value for J1604's disk (Pinilla et al. 2018b). The velocity map is not symmetric with respect to the disk minor axis. Instead the blue-shifted emission occupies more region than the red-shifted counterpart. In addition, the zero velocity line deviates from the minor axis and is twisted in a similar way as the observed CO (3-2) moment-1 map of J1604 (Mayama et al. 2018).

5. SUMMARY & OUTLOOK

In this work, we explore how uneven stellar illuminations influence transition disks. Our 3D hydrodynamic

simulations show that asymmetric shadows, even measured a few percents in depth, drive the disk to become eccentric. This in turns leads to streamline crossing, disk truncation and accretion. We show that this may explain a number of observed oddities of transition disks, including inner edges that are as sharp as allowed by physics, eccentric rings, rapid accretion across the cavity, and twisted velocity maps. In particular, a sharp edge can be carved without the presence of a massive perturber, and a healthy accretion can be driven even in the absence of disk viscosity.

These surprising benefits of shadows are not known before, but they represent perhaps only a small facet of the interesting dynamics in irradiated disks. Many more in-depth studies are needed, even for our particular set-up of a shadowed transition disk. For instance, our crude assumption of a constant lag time should be abandoned. Instead, the disk response to changes in the stellar illumination is more nuanced, with dependencies on factors such as surface density, vertical location, disk flaring, etc. We have also assumed that disk shadows are asymmetric and fixed in inertial space. While supported by available observations, unless we have a first-principle theory for the origin of shadows, these are at best guesses at their characters. Lastly, we need global simulations that span across a larger dynamic range in radius.

Shadows can wreck havoc across a large swath of radial distances, without the need to invoke massive perturbers or disk viscosity. This makes them, in our view, a promising and potent new driver in proto-planetary disks. Targeted observations should be performed to test this theory. The trademark of shadow, as we discover in this work, is the twisted eccentric streamlines.

The authors thank an anonymous referee for many useful comments, and thank Chris Thompson, Norm Murray, Chris Matzner, Janosz Dewberry and Xuening Bai for helpful conversations. They also acknowledge funding from NSERC.

REFERENCES

- ALMA Partnership, Brogan, C. L., Pérez, L. M., et al. 2015, *ApJL*, 808, L3, doi: [10.1088/2041-8205/808/1/L3](https://doi.org/10.1088/2041-8205/808/1/L3)
- Andrews, S. M., Wilner, D. J., Zhu, Z., et al. 2016, *ApJL*, 820, L40, doi: [10.3847/2041-8205/820/2/L40](https://doi.org/10.3847/2041-8205/820/2/L40)
- Antilen, J., Casassus, S., Cieza, L. A., & González-Ruilova, C. 2023, *MNRAS*, 522, 2611, doi: [10.1093/mnras/stad975](https://doi.org/10.1093/mnras/stad975)
- Arce-Tord, C., Casassus, S., Dent, W. R. F., et al. 2023, *MNRAS*, 526, 2077, doi: [10.1093/mnras/stad2885](https://doi.org/10.1093/mnras/stad2885)
- Benisty, M., Stolker, T., Pohl, A., et al. 2017, *A&A*, 597, A42, doi: [10.1051/0004-6361/201629798](https://doi.org/10.1051/0004-6361/201629798)
- Brown, J. M., Blake, G. A., Qi, C., et al. 2009, *ApJ*, 704, 496, doi: [10.1088/0004-637X/704/1/496](https://doi.org/10.1088/0004-637X/704/1/496)
- Calvet, N., D'Alessio, P., Hartmann, L., et al. 2002, *ApJ*, 568, 1008, doi: [10.1086/339061](https://doi.org/10.1086/339061)
- Chiang, E. I., & Goldreich, P. 1997, *ApJ*, 490, 368, doi: [10.1086/304869](https://doi.org/10.1086/304869)

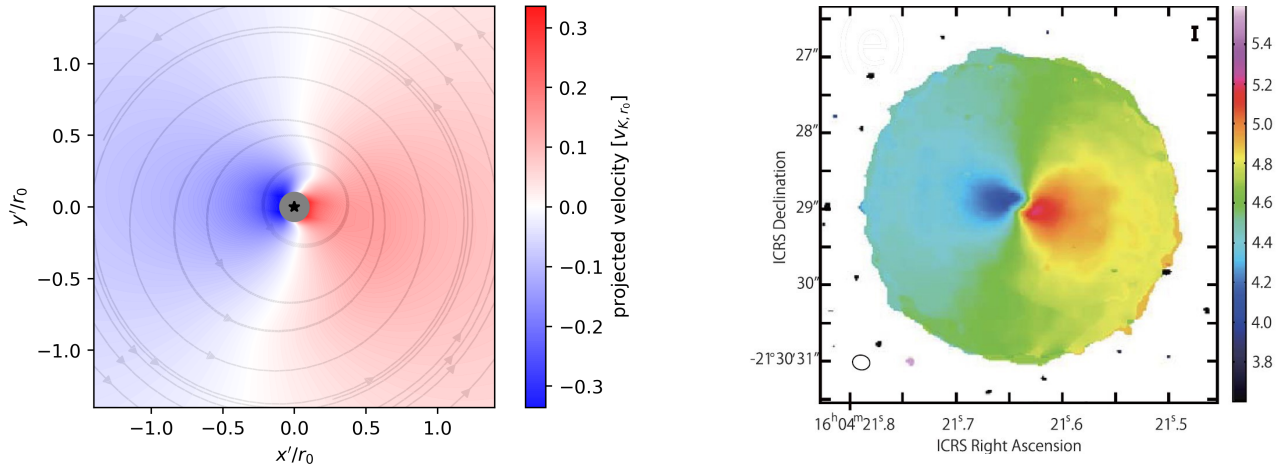


Figure 10. Kinematic signature of a twisted eccentric disk. The left panel shows the projected velocity of our wide ring case ($\sigma_r = 0.3r_0$, $r_0 = 1$, at $t = 250P_0$), with the grey contours indicating the velocity streamlines. The velocity is in unit of circular Keplerian speed at r_0 (~ 3.8 km/s at 60au). The right panel is the moment-1 map of J1604, reproduced from Fig. 1e of [Mayama et al. \(2018\)](#) with permission. The unit on the color bar is km/s. The two are visually comparable.

- Cuello, N., Montesinos, M., Stammler, S. M., Louvet, F., & Cuadra, J. 2019, *A&A*, 622, A43, doi: [10.1051/0004-6361/201731732](https://doi.org/10.1051/0004-6361/201731732)
- Debes, J., Nealon, R., Alexander, R., et al. 2023, *ApJ*, 948, 36, doi: [10.3847/1538-4357/acbdfl](https://doi.org/10.3847/1538-4357/acbdfl)
- Dong, R., van der Marel, N., Hashimoto, J., et al. 2017, *ApJ*, 836, 201, doi: [10.3847/1538-4357/aa5abf](https://doi.org/10.3847/1538-4357/aa5abf)
- Dong, R., Liu, S.-y., Eisner, J., et al. 2018, *ApJ*, 860, 124, doi: [10.3847/1538-4357/aac6cb](https://doi.org/10.3847/1538-4357/aac6cb)
- Duffell, P. C. 2015, *ApJL*, 807, L11, doi: [10.1088/2041-8205/807/1/L11](https://doi.org/10.1088/2041-8205/807/1/L11)
- Espaillet, C., Muzerolle, J., Najita, J., et al. 2014, in *Protostars and Planets VI*, ed. H. Beuther, R. S. Klessen, C. P. Dullemond, & T. Henning, 497–520, doi: [10.2458/azu_uapress.9780816531240-ch022](https://doi.org/10.2458/azu_uapress.9780816531240-ch022)
- Goodman, J., & Rafikov, R. R. 2001, *ApJ*, 552, 793, doi: [10.1086/320572](https://doi.org/10.1086/320572)
- Harsono, D., Long, F., Pinilla, P., et al. 2024, *ApJ*, 961, 28, doi: [10.3847/1538-4357/ad0835](https://doi.org/10.3847/1538-4357/ad0835)
- Huang, J., Andrews, S. M., Dullemond, C. P., et al. 2018, *ApJL*, 869, L42, doi: [10.3847/2041-8213/aaf740](https://doi.org/10.3847/2041-8213/aaf740)
- Jensen, Stanley K., J., Brittan, S. D., Banzatti, A., et al. 2023, arXiv e-prints, arXiv:2312.17218, doi: [10.48550/arXiv.2312.17218](https://doi.org/10.48550/arXiv.2312.17218)
- Juhász, A., & Facchini, S. 2017, *MNRAS*, 466, 4053, doi: [10.1093/mnras/stw3389](https://doi.org/10.1093/mnras/stw3389)
- Kenyon, S. J., & Hartmann, L. 1987, *ApJ*, 323, 714, doi: [10.1086/165866](https://doi.org/10.1086/165866)
- Keyte, L., Kama, M., Booth, A. S., et al. 2023, *Nature Astronomy*, doi: [10.1038/s41550-023-01951-9](https://doi.org/10.1038/s41550-023-01951-9)
- Kurtovic, N. T., Pérez, L. M., Benisty, M., et al. 2018, *ApJL*, 869, L44, doi: [10.3847/2041-8213/aaf746](https://doi.org/10.3847/2041-8213/aaf746)
- Kutra, T., Wu, Y., & Lithwick, Y. 2023, arXiv e-prints, arXiv:2309.16065, doi: [10.48550/arXiv.2309.16065](https://doi.org/10.48550/arXiv.2309.16065)
- Long, Z. C., Akiyama, E., Sitko, M., et al. 2018, *ApJ*, 858, 112, doi: [10.3847/1538-4357/aaba7c](https://doi.org/10.3847/1538-4357/aaba7c)
- Loomis, R. A., Öberg, K. I., Andrews, S. M., & MacGregor, M. A. 2017, *ApJ*, 840, 23, doi: [10.3847/1538-4357/aa6c63](https://doi.org/10.3847/1538-4357/aa6c63)
- Manara, C. F., Testi, L., Natta, A., et al. 2014, *A&A*, 568, A18, doi: [10.1051/0004-6361/201323318](https://doi.org/10.1051/0004-6361/201323318)
- Marino, S., Perez, S., & Casassus, S. 2015, *ApJL*, 798, L44, doi: [10.1088/2041-8205/798/2/L44](https://doi.org/10.1088/2041-8205/798/2/L44)
- Mayama, S., Akiyama, E., Panić, O., et al. 2018, *ApJL*, 868, L3, doi: [10.3847/2041-8213/aae88b](https://doi.org/10.3847/2041-8213/aae88b)
- Montesinos, M., & Cuello, N. 2018, *MNRAS*, 475, L35, doi: [10.1093/mnras/sly001](https://doi.org/10.1093/mnras/sly001)
- Montesinos, M., Perez, S., Casassus, S., et al. 2016, *ApJL*, 823, L8, doi: [10.3847/2041-8205/823/1/L8](https://doi.org/10.3847/2041-8205/823/1/L8)
- Ogilvie, G. I. 2001, *MNRAS*, 325, 231, doi: [10.1046/j.1365-8711.2001.04416.x](https://doi.org/10.1046/j.1365-8711.2001.04416.x)
- Orihara, R., Momose, M., Muto, T., et al. 2023, *PASJ*, 75, 424, doi: [10.1093/pasj/psad009](https://doi.org/10.1093/pasj/psad009)
- Owen, J. E. 2016, *PASA*, 33, e005, doi: [10.1017/pasa.2016.2](https://doi.org/10.1017/pasa.2016.2)
- Papaloizou, J., & Lin, D. N. C. 1984, *ApJ*, 285, 818, doi: [10.1086/162561](https://doi.org/10.1086/162561)
- Pinilla, P., de Boer, J., Benisty, M., et al. 2015, *A&A*, 584, L4, doi: [10.1051/0004-6361/201526981](https://doi.org/10.1051/0004-6361/201526981)
- Pinilla, P., Benisty, M., de Boer, J., et al. 2018a, *ApJ*, 868, 85, doi: [10.3847/1538-4357/aae824](https://doi.org/10.3847/1538-4357/aae824)
- Pinilla, P., Tazzari, M., Pascucci, I., et al. 2018b, *ApJ*, 859, 32, doi: [10.3847/1538-4357/aabf94](https://doi.org/10.3847/1538-4357/aabf94)
- Romanova, M. M., Ustyugova, G. V., Koldoba, A. V., & Lovelace, R. V. E. 2013, *MNRAS*, 430, 699, doi: [10.1093/mnras/sts670](https://doi.org/10.1093/mnras/sts670)

- Rosenfeld, K. A., Chiang, E., & Andrews, S. M. 2014, *ApJ*, 782, 62, doi: [10.1088/0004-637X/782/2/62](https://doi.org/10.1088/0004-637X/782/2/62)
- Shakura, N. I., & Sunyaev, R. A. 1973, *A&A*, 24, 337
- Sheehan, P. D., & Eisner, J. A. 2017, *ApJL*, 840, L12, doi: [10.3847/2041-8213/aa6df8](https://doi.org/10.3847/2041-8213/aa6df8)
- Statler, T. S. 2001, *AJ*, 122, 2257, doi: [10.1086/323713](https://doi.org/10.1086/323713)
- Stone, J. M., Tomida, K., White, C. J., & Felker, K. G. 2020, *The Astrophysical Journal Supplement Series*, 249, 4, doi: [10.3847/1538-4365/ab929b](https://doi.org/10.3847/1538-4365/ab929b)
- Strom, K. M., Strom, S. E., Edwards, S., Cabrit, S., & Skrutskie, M. F. 1989, *AJ*, 97, 1451, doi: [10.1086/115085](https://doi.org/10.1086/115085)
- Su, Z., & Bai, X.-N. 2024, arXiv e-prints, arXiv:2407.12659, doi: [10.48550/arXiv.2407.12659](https://doi.org/10.48550/arXiv.2407.12659)
- Temmink, M., Booth, A. S., van der Marel, N., & van Dishoeck, E. F. 2023, *A&A*, 675, A131, doi: [10.1051/0004-6361/202346272](https://doi.org/10.1051/0004-6361/202346272)
- van der Marel, N. 2023a, *European Physical Journal Plus*, 138, 225, doi: [10.1140/epjp/s13360-022-03628-0](https://doi.org/10.1140/epjp/s13360-022-03628-0)
- . 2023b, *European Physical Journal Plus*, 138, 225, doi: [10.1140/epjp/s13360-022-03628-0](https://doi.org/10.1140/epjp/s13360-022-03628-0)
- van der Marel, N., van Dishoeck, E. F., Bruderer, S., Pérez, L., & Isella, A. 2015a, *A&A*, 579, A106, doi: [10.1051/0004-6361/201525658](https://doi.org/10.1051/0004-6361/201525658)
- . 2015b, *A&A*, 579, A106, doi: [10.1051/0004-6361/201525658](https://doi.org/10.1051/0004-6361/201525658)
- van der Marel, N., van Dishoeck, E. F., Bruderer, S., et al. 2013, *Science*, 340, 1199, doi: [10.1126/science.1236770](https://doi.org/10.1126/science.1236770)
- van der Marel, N., Birnstiel, T., Garufi, A., et al. 2021, *AJ*, 161, 33, doi: [10.3847/1538-3881/abc3ba](https://doi.org/10.3847/1538-3881/abc3ba)
- Walsh, C., Daley, C., Facchini, S., & Juhász, A. 2017, *A&A*, 607, A114, doi: [10.1051/0004-6361/201731334](https://doi.org/10.1051/0004-6361/201731334)
- Wang, L., & Goodman, J. J. 2017, *ApJ*, 835, 59, doi: [10.3847/1538-4357/835/1/59](https://doi.org/10.3847/1538-4357/835/1/59)
- Watanabe, S., & Lin, D. N. C. 2008, in *39th Annual Lunar and Planetary Science Conference, Lunar and Planetary Science Conference*, 1127
- Wu, Y., & Lithwick, Y. 2021, *ApJ*, 923, 123, doi: [10.3847/1538-4357/ac2b9c](https://doi.org/10.3847/1538-4357/ac2b9c)
- Yang, C.-C., & Menou, K. 2010, *MNRAS*, 402, 2436, doi: [10.1111/j.1365-2966.2009.16047.x](https://doi.org/10.1111/j.1365-2966.2009.16047.x)
- Zhu, Z., Nelson, R. P., Hartmann, L., Espaillat, C., & Calvet, N. 2011, *ApJ*, 729, 47, doi: [10.1088/0004-637X/729/1/47](https://doi.org/10.1088/0004-637X/729/1/47)